ACS APPLIED MATERIALS & INTERFACES

www.acsami.org

Research Article

Layer-by-Layer Assembly of Reduced Graphene Oxide and MXene Nanosheets for Wire-Shaped Flexible Supercapacitors

Junyeong Yun, Ian Echols, Paraskevi Flouda, Yijun Chen, Shaoyang Wang, Xiaofei Zhao, Dustin Holta, Miladin Radovic, Micah J. Green, Mohammad Naraghi, and Jodie L. Lutkenhaus*

Cite This: *ACS Appl. Mater. Interfaces* 2021, 13, 14068–14076

Read Online

ACCESS | Metrics & More | Article Recommendations | Supporting Information

ABSTRACT: As the demand for wearable electronic devices increases, interest in small, light, and deformable energy storage devices follows suit. Among these devices, wire-shaped supercapacitors (WSCs) are considered key components of wearable technology due to their geometric similarity to woven fiber. One potential method for creating WSC devices is the layer-by-layer (LbL) assembly technique, which is a "bottom-up" method for electrode fabrication. WSCs require conformal and adhesive coatings of the functional material to the wire-shaped substrate, which is difficult to obtain with other processing techniques such as vacuum filtration or spray-coating. However, the LbL assembly technique produces conformal and robust coatings that can be deposited onto a variety of substrates and shapes, including wires. In this study, we report WSCs made using the LbL assembly of alternating layers of positively charged reduced graphene oxide functionalized with poly(diallyldimethylammonium chloride) and negatively charged $Ti_3C_2T_x$ MXene nanosheets conformally deposited on activated carbon yarns. In this construct, the added LbL film enhances capacitance, energy density, and power density by 240, 227, and 109%, respectively, relative to the uncoated activated carbon yarn, yielding high specific and volumetric capacitances (237 F g^{-1}, 2193 F cm^{-3}). In addition, the WSC possesses good mechanical stability, retaining 90% of its initial capacity after 200 bending cycles. This study demonstrates that LbL coatings on carbon yarns are promising as linear energy storage devices for fibrous electronics.

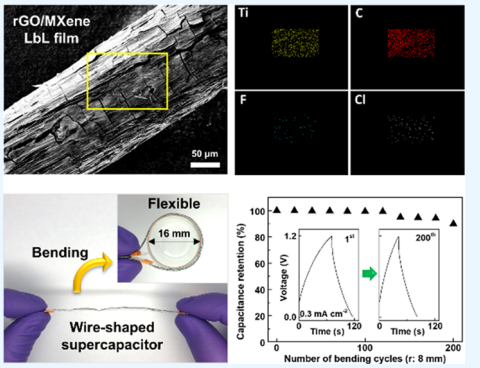

KEYWORDS: *MXene, reduced graphene oxide, layer-by-layer assembly, flexible, wire-shaped supercapacitor*

There is an increasing demand for the development of efficient, flexible, and lightweight energy storage devices such as wire-shaped supercapacitors (WSCs) that can be woven into clothing for wearable electronics.[1−6] More specifically, yarn- or fiber-based supercapacitors and WSCs hold promise,[7−9] but they must function mechanically and electrochemically to meet future demands.[10] In spite of recent reports on WSCs, the production of wire-shaped electrodes with high conductivity, improved capacitance, and flexibility still remains a challenge.

Carbon nanofibers (CNFs) are promising WSC electrode platforms because of their flexibility, high conductivity, and low cost.[11] However, CNFs alone do not provide high capacitance because they rely on a single-charge storage mechanism (electrical double layer at the CNF surface), and the mechanical properties of the fiber need improvement. One way to improve the mechanical stability of individual CNFs is to twist them together to produce carbon yarns (CYs).[12] However, pristine carbon yarns (PCYs) have a low surface area, and thus porous activated carbon yarns (ACYs) have been considered as an alternative, but their capacitance still needs improvement.[13,14] Therefore, we hypothesized that coating ACYs with redox-active materials would improve the overall capacitance while maintaining the desirable configuration offered by the CY base.

To this end, we evaluated 2D transition metal carbides, known as MXenes, because they have recently drawn significant interest for their promising applications in energy storage.[15,16] Among them, $Ti_3C_2T_x$ MXenes have high electrical conductivity (up to 10 000 S cm^{-1}) and excellent volumetric capacity (up to 1500 F cm^{-3}).[17−19] However, pure MXene coatings suffer from poor adhesion,[20] so it is often necessary to add a secondary component. In a previous study, MXene electrodes have included carbon nanotubes and reduced graphene oxide (rGO) as secondary components, but all used a planar configuration not suitable for WSCs.[21,22]

Presently, rGO is of interest for our MXene-based coatings because rGO not only improves adhesion with the MXene-based electrode but also has high electrical conductivity, high

Received: November 2, 2020
Accepted: March 3, 2021
Published: March 17, 2021

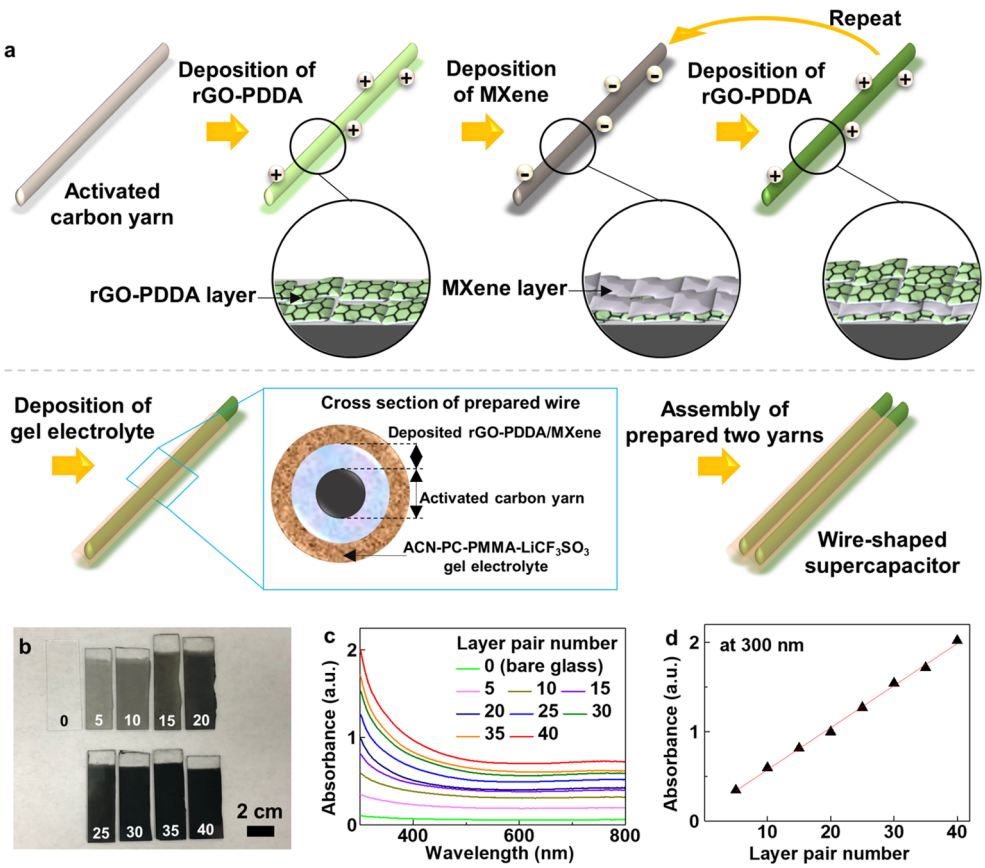

Figure 1. (a) Schematic and cross-sectional view of the fabrication process for wire-shaped rGO-PDDA/MXene supercapacitor. (b) Digital image of multilayer coatings of varying layer pair number on glass substrates. (c) UV−vis spectra of rGO-PDDA/MXene multilayers on glass and (d) absorbance at 300 nm vs layer pair number. An uncoated glass substrate was used as a baseline correction to the UV−vis spectra.

surface area (up to 2675 m^2 g^{-1}), and demonstrated applications in energy storage.[23] Specifically, rGO supercapacitors have capacitances in the range of ∼200 F g^{-1} and operate by an electrical double layer mechanism. In a previous study, rGO and MXene nanosheets have been combined using vacuum filtration to produce supercapacitor electrodes with capacitances of 645 F cm^{-3}.[24] Other works have also combined the two materials using vacuum filtration,[22,25,26] spraying,[27] wet-spinning,[28] or chemical synthesis.[29] However, these methods are not easily translatable to the WSC platform because they do not offer conformal deposition of the functional materials onto wire-shaped substrates. Here, we hypothesized that the layer-by-layer (LbL) assembly would be suitable for depositing rGO and MXene nanosheets onto ACYs for WSCs.

LbL assembly is a sequential adsorption process for materials of complementary electrostatic, hydrogen bonding, or other intermolecular interactions to provide conformal coatings of controllable thickness and structure.[30−34] Besides, LbL assembly can be applied to planar surfaces, spherical particles, inside pores, and surfaces with more complex geometries.[35] Recently, we reported conformal MXene LbL assemblies on nylon fiber, glass, poly(dimethylsiloxane), and poly(ethyleneterepthalate).[20] To-date, there are no reports on MXene-based LbL WSCs with CYs.

In this study, we investigate flexible WSCs composed of conformal LbL coatings of $Ti_3C_2T_x$ MXene and rGO nanosheets on ACYs. We first explore the nature of rGO/MXene LbL growth, monitoring absorbance, thickness, and mass adsorption using ultraviolet−visible (UV−vis) spectroscopy, profilometry, and quartz crystal microbalance (QCM), respectively. In addition, the physicochemical properties of rGO-poly(diallyldimethylammonium chloride) (PDDA)/MXene LbL films are confirmed using X-ray photoelectron spectroscopy (XPS), Raman spectroscopy, and X-ray diffraction (XRD). The morphology of the LbL-coated ACY (LACY) is revealed using scanning electron microscopy (SEM). We next explore the electrochemical properties of LACY and WSCs using aqueous, nonaqueous, and gel electrolytes, respectively. We compare PCYs, ACYs, and LACYs to show that the electrochemical performance was significantly improved with the rGO-PDDA/MXene coatings. Finally, we observe that all solid-state LACY WSCs have excellent mechanical stability, maintaining stable performance over repeated bending cycles.

Figure 1 shows a schematic illustration of the LbL assembly of positively charged rGO-PDDA and negatively charged MXene nanosheets onto ACYs. Positively charged rGO-PDDA was obtained by adding PDDA and hydrazine to a GO dispersion. The ACYs were alternately immersed in the rGO-PDDA and MXene dispersions, followed by drying and then more cycles of LbL assembly to build up the desired number of layer pairs (LPs), resulting in LbL-coated ACYs (LACYs). Additionally, we deposited analogous films on glass (Figure 1b) and ITO-coated glass substrates (Figure S1) for further characterization. The five LP rGO-PDDA/MXene multilayer films appeared pale gray and became visibly darker as the number of LPs increased to 40. This was confirmed using

https://doi.org/10.1021/acsami.0c19619
ACS Appl. Mater. Interfaces 2021, 13, 14068−14076

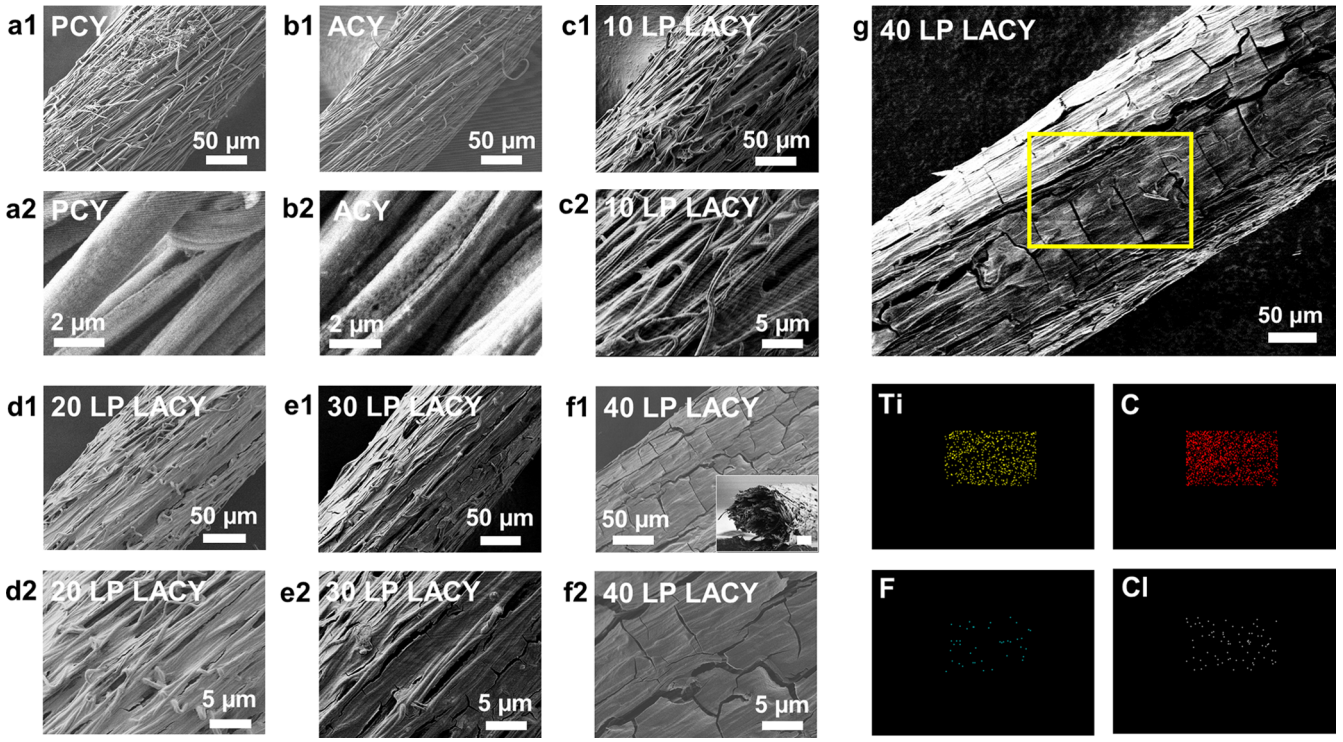

Figure 2. SEM images of (a) PCY, (b) ACY, (c) 10 LP, (d) 20 LP, (e) 30 LP, and (f) 40 LP LACYs. (g) Elemental mapping images obtained from the yellow square in the surface image of a 40 LP LACYs: (yellow) titanium, (red) carbon, (green) fluorine, and (white) chlorine.

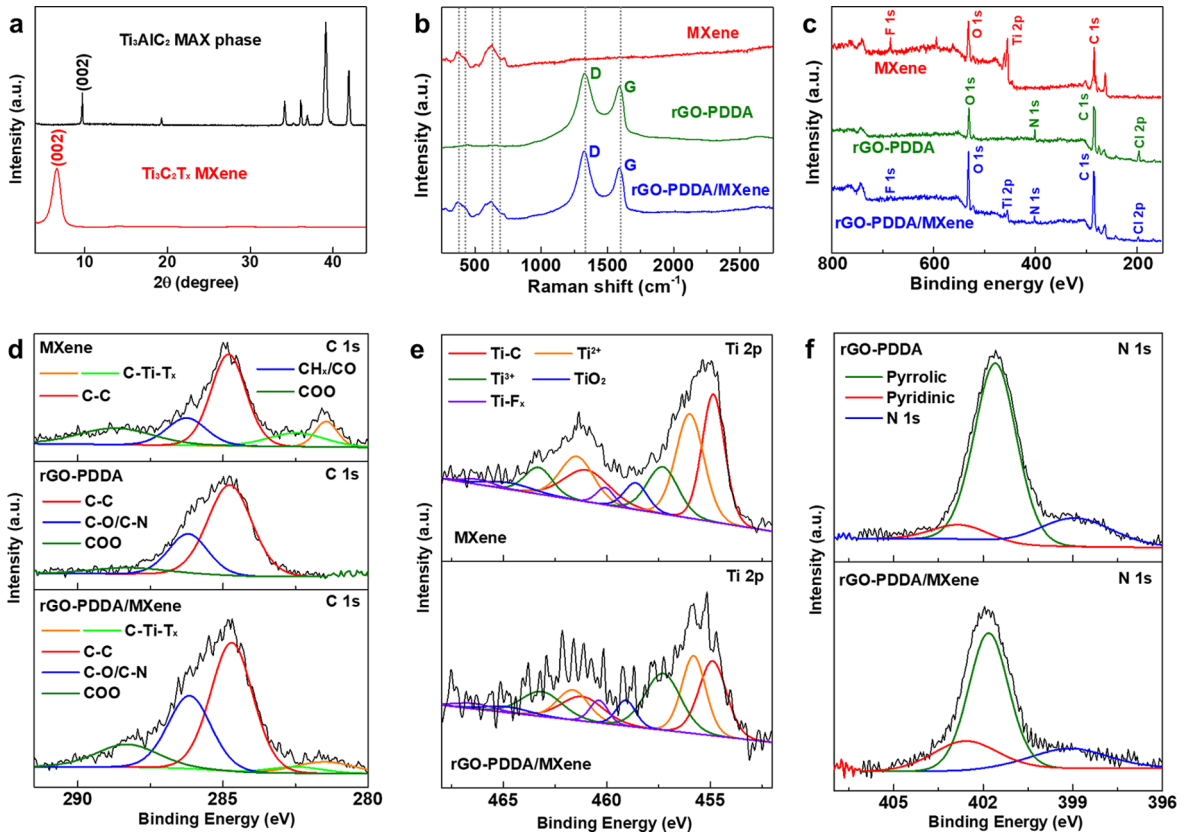

Figure 3. (a) X-ray diffraction patterns of (black) the Ti_3AlC_2 MAX phase and (red) $Ti_3C_2T_x$ MXenes. (e) Raman spectra of (red) MXenes, (green) rGO-PDDA, and (blue) rGO-PDDA/MXene multilayer. (c) XPS survey spectra of (red) MXenes, (green) rGO-PDDA, and (blue) rGO-PDDA/MXene multilayer and the component peak fits for (d) C 1s, (e) Ti 2p, and (f) N 1s.

https://doi.org/10.1021/acsami.0c19619
ACS Appl. Mater. Interfaces 2021, 13, 14068−14076

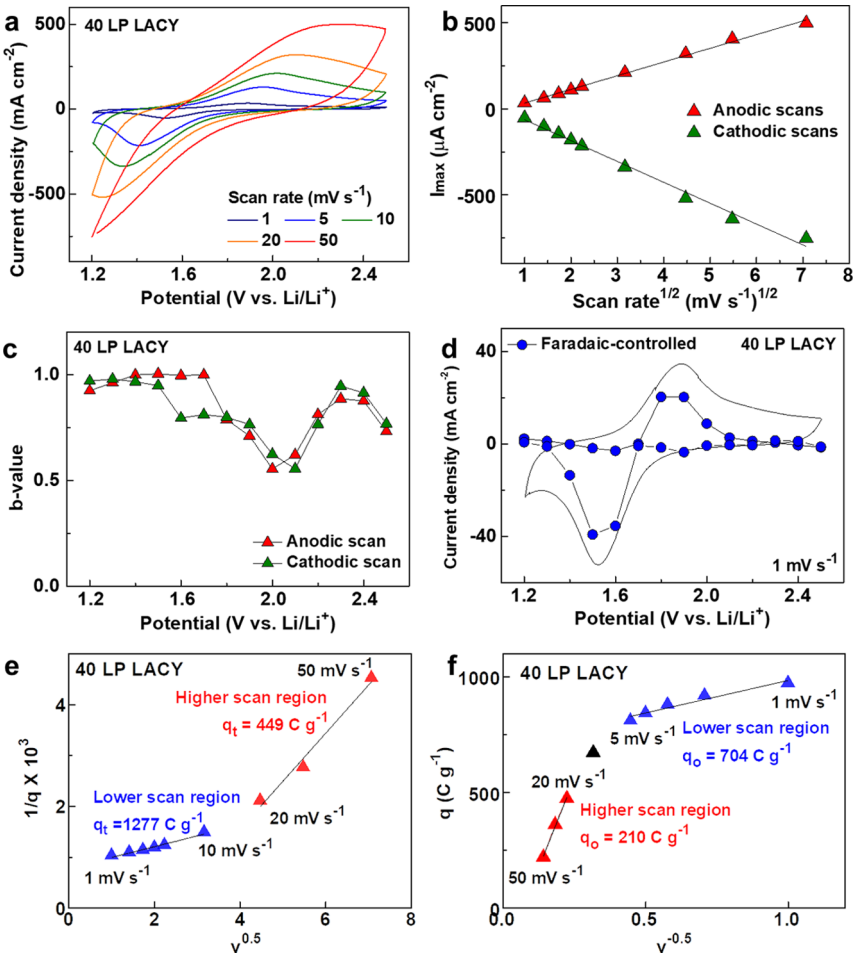

Figure 4. Cyclic voltammetry analysis of 40 LP LACYs (rGO-PDDA/MXene on a carbon yarn). (a) Cyclic voltammograms at various scan rates. (b) Maximum current vs (scan rate)$^{1/2}$ taken from the corresponding cyclic voltammograms. (c) Calculated *b*-values for anodic and cathodic scans vs voltage (*b*-values were obtained from the equation $I = av^b$ from 1 to 5 mV s^{-1}). (d) Faradaic-controlled contribution is separated from a cyclic voltammogram at 1 mV s^{-1}. The blue dotted line indicates the faradaic-controlled redox process, and the solid line indicates the total current. (e) $1/q$ vs $\nu^{0.5}$ for q_t, and (f) q vs $\nu^{-0.5}$ for q_o for 40 LP LACYs of rGO-PDDA/MXene. (Three-electrode cell: lithium ribbons as counter and reference electrodes; 0.5 M $LiCF_3SO_3$ dissolved in propylene carbonate as an electrolyte).

UV−vis spectroscopy, in which the absorbance increased linearly with the number of LPs (Figure 1c,d). From QCM (Figure S2), a linear increase in mass (0.94 μg cm^{-2} per LP) also confirmed this trend, and the mass fraction of rGO-PDDA and MXene layers was 32 and 68 wt %, respectively. Figures S3 and S4 show changes in thickness and roughness with increasing LP numbers. The thickness increased linearly as ~8 nm per LP. These results indicate that the adjustment of the LP number allows for the precise control of the multilayer's mass, thickness, and roughness.

Figure 2 shows the SEM images of PCY, ACY, and 10−40 LP LACY morphologies. Figure 2a1,a2 shows surface SEM images of a PCY, which consisted of smooth carbon strands with diameters ranging from 1.3 to 2.2 μm. Figure 2b1,b2 shows an ACY with a slightly porous structure from activation, similar to previous findings.[14] We also observed that as the number of LPs increased from 10 to 40 LPs, the coating gradually deposited first at the ACY interior and finally on the exterior (Figure 2c−g). Finally, Figure 2f1,f2 shows the 40 LP LACYs, in which the rGO-PDDA/MXene film covered the ACY; the cracks were a result of coating shrinkage during drying and were not observed in undried LACYs (Figure S5). The yellow square in Figure 2g shows EDS elemental mapping of elements constituting rGO-PDDA and MXene nanosheets for 40 LP LACYs. These images, along with cross-sections (Figures S6 and S7), indicate that rGO-PDDA/MXene multilayers were present not only on the outside of the yarn but also on the inside.

Figure 3a shows the XRD patterns of the MAX phase and drop-cast $Ti_3C_2T_x$ MXene nanosheets. At a 2θ angle of 9.8°, a pronounced peak (002) of the MAX phase appeared, which was shifted to 6.6° for the $Ti_3C_2T_x$ MXene nanosheets. This is consistent with the conversion of the MAX phase to MXene nanosheets, indicated by the increase in the (002) d-spacing and broadening of the peak.[36] Figure 3b shows the Raman spectra of drop-cast MXene and rGO-PDDA nanosheets, as well as rGO-PDDA/MXene multilayers. In the MXene's Raman spectrum, peaks attributed to the $Ti_3C_2(OH)_2$ in-plane mode at 280 and 627 cm^{-1} and the $Ti_3C_2F_2$ E_g mode at 612 cm^{-1} were observed.[37] The MXene's Raman spectra also exhibited peaks associated with titanium oxides (rutile phase) at 382 and 617 cm^{-1}.[38] The rGO-PDDA spectra exhibited signature D- and G-bands (1324 and 1590 cm^{-1}, respectively)[39] with an intensity ratio of 1.15 that was higher than that of GO itself (I_D/I_G: 0.84, Figure S8), which was attributed to defects that occurred during the reduction process.[40] In the

https://doi.org/10.1021/acsami.0c19619
ACS Appl. Mater. Interfaces 2021, 13, 14068−14076

rGO-PDDA/MXene multilayer, signatures of both materials were observed.

XPS analysis was also performed to confirm the chemical states of drop-cast MXenes, drop-cast rGO-PDDA nanosheets, and the rGO-PDDA/MXene multilayer. Figure 3c shows XPS survey spectra, in which the Ti 2p and N 1s peaks were observed, and Figure 3d shows the respective deconvoluted C 1s spectra. The rGO-PDDA/MXene C 1s spectra show C-Ti-T_x generated from the MXene and C−N generated from rGO-PDDA, which confirms again that both species were present in the final LACY. The detailed position and full width at half-maximum of peaks are listed in Tables S1−S3. This analysis confirms the mutual presence of rGO-PDDA and MXene nanosheets in the rGO-PDDA/MXene multilayer.

Before measuring the electrochemical performance of WSC devices, we first evaluated the electrochemical properties of the rGO-PDDA/MXene multilayers alone (without contributions from the CY base, Figure S9 and Table S4) as a function of LP number in aqueous electrolyte. As the number of LPs increased, the areal capacitance increased; the 40 LP rGO-PDDA/MXene multilayer exhibited the highest capacitance of 13.8 mF cm^{-2} and was selected as the optimal LP number. We next compared the capacitance and impedance response of PCY, ACY, and 40 LP LACYs in a three-electrode cell in either 3 M LiCl (Figure S10 and Table S5) or 1 M H_2SO_4 (Figure S11 and Table S6). When LiCl is the electrolyte, the areal capacitance was highest for 40 LP LACYs, followed by ACY and then PCY. Specifically, ACY's capacitance was 1500% higher than that of PCY, and that of LACY was 162% higher than that of ACY. Activation enhances the surface area and the carbon yarn's hydrophilicity,[14] and the LbL coating greatly enhances capacitance. Further, the 40 LP LACYs exhibited the lowest ESR as compared to PCY and ACY. The trends were similar for the case of 1 M H_2SO_4 as the electrolyte.

We next turn to the prospect of nonaqueous electrolytes because they provide a larger voltage window of operation. $LiCF_3SO_3$ in propylene carbonate was selected as the electrolyte because of its past application to supercapacitors and batteries, in which charge storage is facilitated by Li^+ ion exchange in the active material.[41,42] Here, we compared the basic electrochemical response of several electrodes to identify the role of the LbL processing method in the performance. Specifically, we compared spray-coated rGO-PDDA, MXene, and rGO-PDDA/MXene electrodes with 10 LP LbL-assembled rGO-PDDA/MXene multilayers (all of the similar thickness, ∼70 nm). Figure S12 shows and discusses the results. For the spray-coated rGO-PDDA/MXene electrode, the composition was matched with that of the LbL assembly, as determined using QCM (Figure S2). In all cases, the LbL electrode performed significantly better. Specifically, the LbL electrode showed an areal capacitance 150% higher than that of the comparable spray-coated electrode having the same composition. We attribute the improved performance to the tight packing of the nanomaterials brought about by the LbL processing method.

Then, the mechanism of charge storage in the nonaqueous electrolyte was analyzed using the cyclic voltammetry of 40 LP rGO-PDDA/MXene on ACY at varying scan rates (1, 5, 10, 20, and 50 mV s^{-1}) to calculate *b*-values, quantify the faradaic contribution, and separate the charge stored at inner and outer surfaces. A three-electrode cell was employed, using 40 LP LACYs as a working electrode, lithium ribbons as counter and reference electrodes, and 0.5 M $LiCF_3SO_3$ dissolved in propylene carbonate as an electrolyte. The cyclic voltammograms, shown in Figure 4a, exhibit a pair of peaks (1.87/1.53 V) that are characteristic of a Li^+ ion intercalation processes.[43] A plot of the maximum current vs (scan rate)$^{1/2}$ indicates a diffusion-controlled reaction (Figure 4b). To analyze the charge storage mechanism of rGO-PDDA/MXene LACY in more detail, we used the following equation to calculate *b*-values at particular voltages[44]

$$i_d = av^b \quad (1)$$

where i_d is the current density at a particular voltage (A cm^{-2}), v is the scan rate (mV s^{-1}), and a and b are fitted parameters. If b is 0.5, the redox process is considered an ideal faradaic process, and if b = 1, the redox process is regarded as an ideal non-faradaic process. Figure 4c shows the *b*-values calculated for each potential (Figure S14). In general, the *b*-values are near unity, except for b approaching 0.5 near 2.0 V. The relative contribution of faradaic and non-faradaic charge storage was deconvoluted by the following

$$i_t = a_1 v + a_2 v^{0.5} \quad (2)$$

where i_t denotes the total current, and a_1 and a_2 represent the relative contribution of non-faradaic and faradaic charge storage processes, respectively. Figure 4d shows the faradaic portion (blue dots) close to the total cyclic voltammogram (solid line) at a scan rate of 1 mV s^{-1} (Figure S15). The faradaic portion overlapped with the redox peaks, again confirming diffusion-limited transport of Li^+ ions.

In general, a three-dimensional structure may store charge at inner or outer layers according to the time scale of the reaction (e.g., scan rate).[45] More specifically, at shorter time scales, the charge is stored at outer layers, and at longer time scales, inner layers become accessible. Therefore, we calculated the total maximum charge (q_t) and a fraction of charge stored at the inner (q_i) and outer surfaces (q_o) using the following equation

$$q_t = q_i + q_o \quad (3)$$

The values for q_t and q_o are each obtained from intercepts of $1/q$ vs $v^{0.5}$ (Figure 4e) and q vs $v^{-0.5}$ (Figure 4f), respectively, taken from the cyclic voltammogram of 40 LP LACYs. We identified two regions of charge storage behavior. The q_t value at low scan rates (1−10 mV/s) was more than double the value at high scan rates (20−50 mV/s), indicating that more charge is stored in longer time-scale processes. In general, q_i was ∼50% of q_t. Together, these results support that charge occurs in inner and outer layers with diffusion control being a contributing factor.

Then, we investigated the electrochemical properties of WSCs using PCYs, ACYs, and LACYs in two-electrode symmetric cells. We used a solid gel electrolyte containing acetonitrile, propylene carbonate, poly(methyl methacrylate), and $LiCF_3SO_3$ (ACN-PC-PMMA-$LiCF_3SO_3$) to fabricate all solid-state WSCs; see Table S7. This solid gel system was selected for its excellent chemical stability[41] and high ionic conductivity (3.93×10^{-6} S cm^{-1}).[46] Further details of the surface area of the two electrodes, gel layer, and the entire device, as well as calculation methods, are given in Figure S16 and Table S8.

We first considered the effects on the capacitance from varying the number of LPs, followed by varying the length of the WSCs. As shown in Figure S17, the 40 LP LACY WSCs showed the highest areal capacitance out of the range

https://doi.org/10.1021/acsami.0c19619
ACS Appl. Mater. Interfaces 2021, 13, 14068−14076

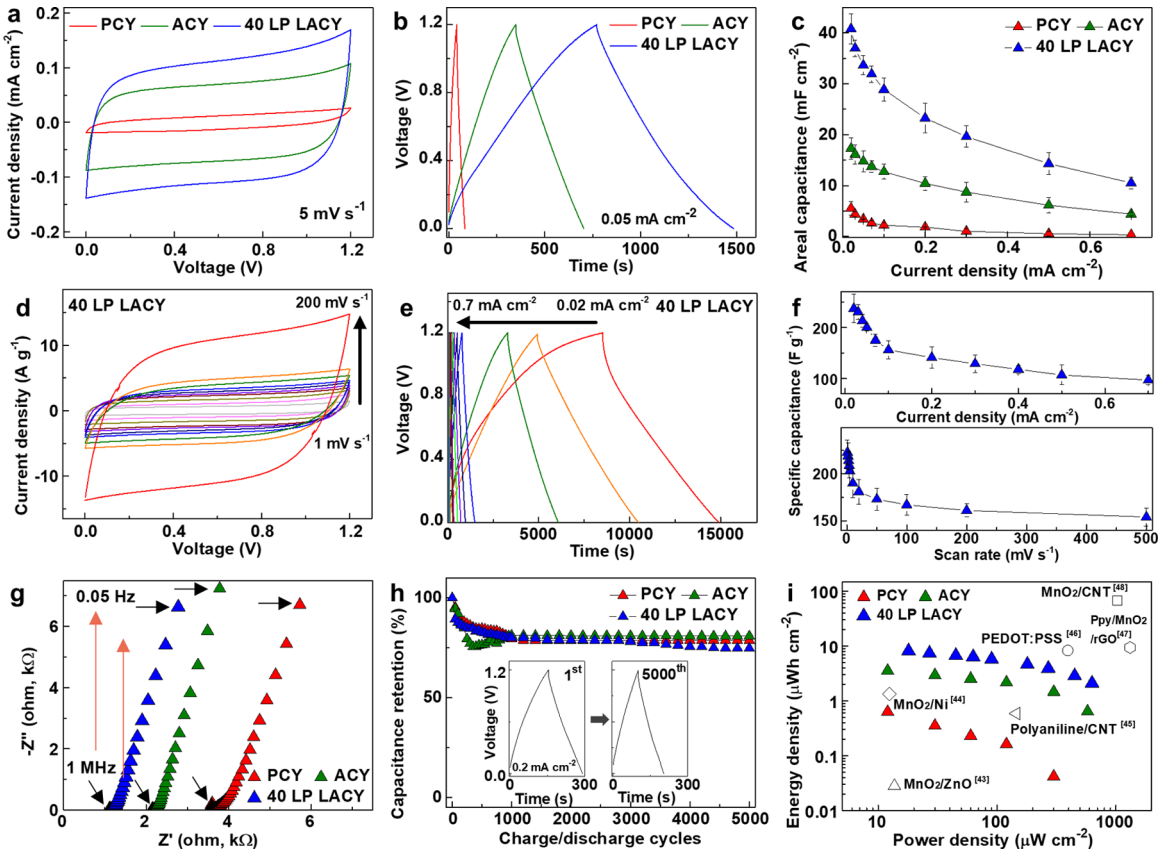

Figure 5. Electrochemical performance of WSCs for (red) PCYs, (green) ACYs, and (blue) 40 LP LACYs. (a) CV curves at a scan rate of 5 mV s^{-1}. (b) Galvanostatic charge−discharge curves at a current density of 0.05 mA cm^{-2}. (c) Areal capacitance from 10 different WSCs with error bars. (d) CV curves at various scan rates. (e) Galvanostatic charge−discharge curves at various current densities. (f) Specific capacitances at various current densities and at various scan rates from 10 different WSCs with error bars. (g) Nyquist impedance plots. (h) Capacitance retention over 5000 charge−discharge cycles at a current density of 0.2 mA cm^{-2}. The inset shows the charge−discharge curves for the 1st and 5000th cycles. (i) Ragone plot. The device consisted of symmetric wire electrodes and a gel electrolyte composed of ACN-PC-PMMA-$LiCF_3SO_3$.

investigated (10−55 LPs). This result indicates some balance between the added capacitance from increasing the multilayer thickness vs the increased ion-diffusion limitation as the number of LPs increases. This result was consistent with our findings regarding the aqueous electrolyte in a three-electrode cell, described earlier. As shown in Figure S18, as the WSC length was varied from 1 to 5 cm, the areal capacitance remained constant, indicating that the length of the WSC does not affect the performance. Given these considerations, WSCs composed of 40 LP rGO-PDDA/MXene on 5 cm long LACY were selected for further investigation.

We next compared the cyclic voltammetry (CV) response for PCYs, ACYs, and 40 LP LACYs. The CVs (Figure 5a) at a scan rate of 5 mV s^{-1} are nearly rectangular in the voltage range of 0−1.2 V, indicating capacitive behavior and good reversibility with no noticeable redox peaks.[47] For higher scan rates (100 and 500 mV s^{-1}, Figure S19), the CV responses for PCY and ACY WSCs became distorted; however, the 40 LP LACY WSCs maintained a rectangular CV curve and showed relatively stable reversibility.

In Figure 5b, the galvanostatic charge−discharge curves at a current density of 0.05 mA cm^{-2} had a triangular shape, confirming the dominant capacitive properties for this device configuration. The charge−discharge responses at other current densities (0.02 and 0.7 mA cm^{-2}, Figure S20) were also triangular in shape. From the galvanostatic charge−discharge response, we plotted the areal capacitances for each current density investigated (Figure 5c). The areal capacitance of 40 LP LACYs (40.8 mF cm^{-2} at a current density of 0.02 mA cm^{-2}) was ∼2.4 times greater than that of ACY and ∼7.4 times greater than that of PCY.

Figure 5d shows the CV response for various scan rates for 40 LP LACY WSCs. These CV curves exhibited a rectangular shape with no distinct redox peaks, which indicates good capacitive behavior regardless of the scan rate. Similarly, Figure 5e shows the galvanostatic charge−discharge response at various current densities. The linear charge−discharge profiles signify symmetrical charge−discharge properties and excellent capacitive. The specific capacitances from the CV and galvanostatic charge−discharge curves are summarized in Figure 5f.

Impedance spectra in Figure 5g show that the equivalent series resistance (ESR) values of PCY, ACY, and 40 LP LACY WSCs were 3.6, 2.2, and 1.2 kΩ, respectively. As shown in Figure S21, we compared the impedance spectra of PCY, ACY, and 40 LP rGO-PDDA/MXene LACY WSCs using PC-$LiCF_3SO_3$ liquid electrolyte and ACN-PC-PMMA-$LiCF_3SO_3$ gel electrolyte. Figure S21 shows lower ESR values for the case of a liquid electrolyte (210−725 Ω). These results demonstrate that the higher ESR values of PCY, ACY, and 40 LP WSCs originate from the gel electrolyte. Together, these results confirm the benefit of the rGO-PDDA/MXene coating on the CY, in which capacitance dramatically improves and ESR decreases. Notably, the standard deviation in capacitance for

https://doi.org/10.1021/acsami.0c19619
ACS Appl. Mater. Interfaces 2021, 13, 14068−14076

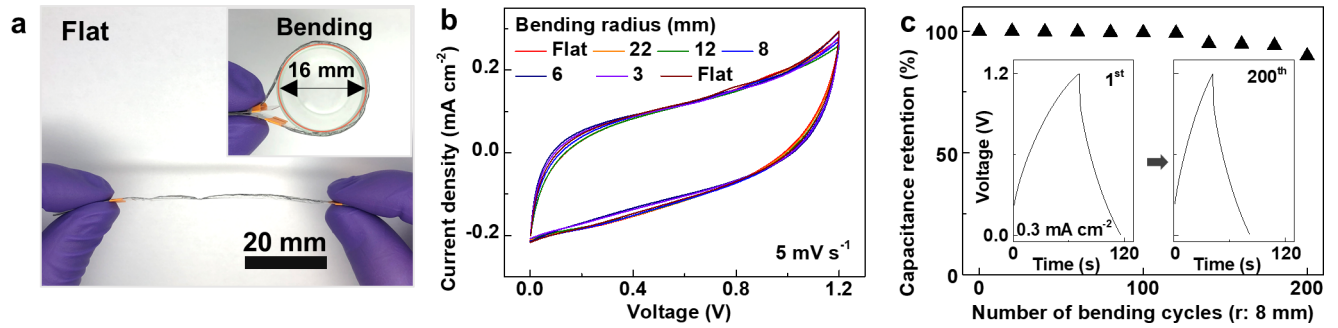

Figure 6. Mechanical stability test of 40 LP LACY WSCs. (a) Digital images of 40 LP LACY WSCs in flat and (inset) bent states. (b) CV curves at varying bending radii. (c) Capacitance retention with an increasing number of bending cycles (bending radius: 8 mm). The inset shows the charge−discharge curves after the 1st and 200th bending cycles.

10 WSCs was relatively small, demonstrating device-to-device reproducibility.

Then, Figure 5h shows the capacitance retention measured over 5,000 charge−discharge cycles for each WSC, in which PCY, ACY, and 40 LP LACY WSCs retained 79, 81, and 75%, respectively, of their initial capacitance. The inset in Figure 5h shows the 1st and the 5000th charge−discharge cycle for the 40 LP LACY WSCs, in which the triangular shape was retained, indicating stable capacitive behavior. We note that capacitance largely drops in the first few hundred cycles but remains very steady after that. This is an indication of good stability after the first cycles. Further, to examine the self-discharge behavior, we charged each WSC to 1.2 V and observed the cell potential for 10 h (Figure S22). After 30 min of resting, the cell potentials all decreased to 0.6 V. The cell potential further declined after 10 h of resting, but none of the WSCs completely self-discharged. The final resting potential for the 40 LP LACY WSCs was 0.57 V.

From the galvanostatic charge−discharge experiments, the energy density (E, Wh cm^{-2}) and power density (P, W cm^{-2}) were calculated and summarized in a Ragone plot (Figure 5i). The performances of PCY, ACY, and 40 LP LACY WSCs were compared with previous WSCs from the literature.[48−53] We restricted our representation to an areal basis because the 40 LP multilayer are very thin (~300 nm). For thin coatings such as these, it has been recommended to use an areal basis to avoid overestimating the proper performance metrics.[54] Forty LP LACY WSCs had a maximum energy density of 8.2 μWh cm^{-2} and a maximum power density of 630.1 μW cm^{-2}. The addition of the 40 LP rGO-PDDA/MXene multilayers to the activated carbon yarn manifested as a 227% improvement in energy and a 109% improvement in power at a current density of 0.02 mA cm^{-2} relative to the uncoated ACY. In addition, we compared the capacitance, electrode diameter, electrolyte, and voltage window of previously reported non-MXene/non-rGO-based WSCs, rGO-based WSCs, and MXene-based WSCs with the fabricated 40 LP LACY WSCs (Table S9). In particular, our rGO-PDDA/MXene WSC has a wider voltage range (1.2 V) and superior areal capacitance (40.8 mF cm^{-2}), specific capacitance (237 F g^{-1}), and volumetric capacitance (2193 F cm^{-3}) compared to the previous rGO-based and MXene-based WSCs.

Then, we examined the flexibility of 40 LP LACYs by applying gel electrolyte to a single LACY (Figures S23 and S24, Figure 6a). The mechanical properties (Young's modulus and tensile strength) of PCY, ACY, and LACY are presented in Figure S25. Without the gel electrolyte, the CYs were brittle and broke easily upon handling, but a single LACY with gel electrolyte maintained stable resistance values regardless of the bending radii. There were no noticeable changes in the CV or the charge−discharge responses during bending at varying radii for the 40 LP LACY WSCs (Figures 6b and S26), indicating that our WSCs were mechanically stable up to a bending radius of at least 3 mm. Figure 6c shows the capacitance retention of a WSC alternating between flat and bent states (8 mm bending radius), which is equal to a maximum axial strain of ~1.1% (see the calculation in the SI), in which 90% of the initial capacitance was maintained after 200 bending tests.

CONCLUSIONS

This study demonstrated that the low capacitance, energy density, and power density of CYs could be dramatically improved by activating and coating them with rGO-PDDA/MXene multilayers, thus enabling their application for WSCs. The growth of the rGO-PDDA/MXene LbL film was linear and conformal even within the CY structure. The thickness of the rGO-PDDA/MXene LbL film was controlled by the number of layer pairs deposited (8 nm/LP), demonstrating the tunability of the approach. Symmetric gel-based WSCs proved that the added rGO-PDDA/MXene LbL film enhanced capacitance, energy, and power by 240, 227, and 109%, respectively, relative to the uncoated ACY. In particular, the LACY WSC had an excellent areal capacitance (40.8 mF cm^{-2}), volumetric capacitance (2193 F cm^{-3}), and specific capacitance (237 F g^{-1}) with a wide voltage range (0−1.2 V) compared to the existing graphene-based and MXene-based WSCs. Further, these WSCs withstood 200 cycles of bending while maintaining their electrochemical performance. Looking to the future, the carbon yarn platform is more broadly promising due to the outstanding mechanical properties arising from the carbon yarn base.

ASSOCIATED CONTENT

Supporting Information

The Supporting Information is available free of charge at https://pubs.acs.org/doi/10.1021/acsami.0c19619.

Detailed experimental methods; calculation equation for surface area and volume, capacitance, energy density, and power density; QCM data analysis, profilometric data analysis, AFM data, surface SEM images, and elemental mapping of LACY; Raman spectra of GO and rGO-PDDA; XRD patterns of the Ti_3AlC_2 MAX phase and $Ti_3C_2T_x$ MXenes; XPS spectra of rGO-PDDA, MXene, and rGO-PDDA/MXenes; three-electrode cell

https://doi.org/10.1021/acsami.0c19619
ACS Appl. Mater. Interfaces 2021, 13, 14068−14076

performance; and mechanical properties of PCY, ACY, and LACY (PDF)

AUTHOR INFORMATION

Corresponding Author

Jodie L. Lutkenhaus − *Artie McFerrin Department of Chemical Engineering and Department of Materials Science and Engineering, Texas A&M University, College Station, Texas 77843, United States;* orcid.org/0000-0002-2613-6016; Email: jodie.lutkenhaus@tamu.edu

Authors

Junyeong Yun − *Artie McFerrin Department of Chemical Engineering, Texas A&M University, College Station, Texas 77843, United States*

Ian Echols − *Artie McFerrin Department of Chemical Engineering, Texas A&M University, College Station, Texas 77843, United States*

Paraskevi Flouda − *Department of Materials Science and Engineering, Texas A&M University, College Station, Texas 77843, United States*

Yijun Chen − *Department of Aerospace Engineering, Texas A&M University, College Station, Texas 77843, United States*

Shaoyang Wang − *Artie McFerrin Department of Chemical Engineering, Texas A&M University, College Station, Texas 77843, United States*

Xiaofei Zhao − *Artie McFerrin Department of Chemical Engineering, Texas A&M University, College Station, Texas 77843, United States;* orcid.org/0000-0002-0593-8490

Dustin Holta − *Department of Materials Science and Engineering, Texas A&M University, College Station, Texas 77843, United States*

Miladin Radovic − *Department of Materials Science and Engineering, Texas A&M University, College Station, Texas 77843, United States*

Micah J. Green − *Artie McFerrin Department of Chemical Engineering and Department of Materials Science and Engineering, Texas A&M University, College Station, Texas 77843, United States;* orcid.org/0000-0001-5691-0861

Mohammad Naraghi − *Department of Aerospace Engineering, Texas A&M University, College Station, Texas 77843, United States;* orcid.org/0000-0002-1841-7598

Complete contact information is available at: https://pubs.acs.org/10.1021/acsami.0c19619

Author Contributions

J.Y.—Carried out the majority of the experiments and wrote the manuscript and supporting information drafts. I.E.—Carried out the optimization of the LbL assembly conditions and analysis of the state of the LbL assembled film. P.F.—Carried out XPS and SEM analysis. Y.C.—Carried out synthesis of pristine and activated carbon yarns. S.W.—Carried out analysis of the charge storage mechanism using the three electrode measurement system. X.Z.—Carried out synthesis of $Ti_3C_2T_x$ MXene nanosheets. D.H.—Carried out synthesis of Ti_3AlC_2MAX phase. M.R.—Carried out management of MAX phase synthesis and optimization of its properties. M.J.G.—Carried outmanagement of MXene nanosheets synthesis and optimization of its properties. M.N.—Carried out management ofpristine carbon yarn and activated carbon yarn synthesis and optimization of its properties.

Notes

The authors declare no competing financial interest.

ACKNOWLEDGMENTS

This material is based in part upon the work supported by the National Science Foundation under Grant 1760859. The authors acknowledge the Air Force Office of Scientific Research for supporting this work under the award number FA9550-15-1-0170 and seed grant funding from Texas A&M Energy Institute and the T3 TAMU program. The authors also thank Ahmad Amiri for the CYs.

REFERENCES

(1) Gogotsi, Y. Energy Storage Wrapped up. *Nature* **2014**, *509*, 568−569.

(2) Jost, K.; Dion, G.; Gogotsi, Y. Textile Energy Storage in Perspective. *J. Mater. Chem. A* **2014**, *2*, 10776−10787.

(3) Hu, L.; Pasta, M.; La Mantia, F.; Cui, L.; Jeong, S.; Deshazer, H. D.; Choi, J. W.; Han, S. M.; Cui, Y. Stretchable, Porous, and Conductive Energy Textiles. *Nano Lett.* **2010**, *10*, 708−714.

(4) Ren, J.; Zhang, Y.; Bai, W.; Chen, X.; Zhang, Z.; Fang, X.; Weng, W.; Wang, Y.; Peng, H. Elastic and Wearable Wire-Shaped Lithium-Ion Battery with High Electrochemical Performance. *Angew. Chem., Int. Ed.* **2014**, *53*, 7864−7869.

(5) Zhai, S.; Karahan, H. E.; Wang, C.; Pei, Z.; Wei, L.; Chen, Y. 1D Supercapacitors for Emerging Electronics: Current Status and Future Directions. *Adv. Mater.* **2020**, *32*, No. 1902387.

(6) Zhai, S.; Wang, C.; Karahan, H. E.; Wang, Y.; Chen, X.; Sui, X.; Huang, Q.; Liao, X.; Wang, X.; Chen, Y. Nano-RuO_2-Decorated Holey Graphene Composite Fibers for Micro-Supercapacitors with Ultrahigh Energy Density. *Small* **2018**, *14*, No. 1800582.

(7) Yang, Z.; Deng, J.; Chen, X.; Ren, J.; Peng, H. A Highly Stretchable, Fiber-Shaped Supercapacitor. *Angew. Chem., Int. Ed.* **2013**, *52*, 13453−13457.

(8) Pu, X.; Li, L.; Liu, M.; Jiang, C.; Du, C.; Zhao, Z.; Hu, W.; Wang, Z. L. Wearable Self-Charging Power Textile Based on Flexible Yarn Supercapacitors and Fabric Nanogenerators. *Adv. Mater.* **2016**, *28*, 98−105.

(9) Yu, D.; Qian, Q.; Wei, L.; Jiang, W.; Goh, K.; Wei, J.; Zhang, J.; Chen, Y. Emergence of Fiber Supercapacitors. *Chem. Soc. Rev.* **2015**, *44*, 647−662.

(10) Senthilkumar, S. T.; Kim, J.; Wang, Y.; Huang, H.; Kim, Y. Flexible and Wearable Fiber Shaped High Voltage Supercapacitors Based on Copper Hexacyanoferrate and Porous Carbon Coated Carbon Fiber Electrodes. *J. Mater. Chem. A* **2016**, *4*, 4934−4940.

(11) Chen, L.-F.; Huang, Z.-H.; Liang, H.-W.; Yao, W.-T.; Yu, Z.-Y.; Yu, S.-H. Flexible All-solid-state High-power Supercapacitor Fabricated with Nitrogen-doped Carbon Nanofiber Electrode Material Derived from Bacterial Cellulose. *Energy Environ. Sci.* **2013**, *6*, 3331−3338.

(12) Gao, L.; Li, X.; Li, X.; Cheng, J.; Wang, B.; Wang, Z.; Li, C. A Coaxial Yarn Electrode Based on Hierarchical MoS_2 Nanosheets/carbon Fiber Tows for Flexible Solid-state Supercapacitors. *RSC Adv.* **2016**, *6*, 57190−57198.

(13) Hu, Z.; Srinivasan, M. P. Mesoporous High-surface-area Activated Carbon. *Microporous Mesoporous Mater.* **2001**, *43*, 267−275.

(14) Chen, Y.; Amiri, A.; Boyd, J. G.; Naraghi, M. Promising Trade-Offs Between Energy Storage and Load Bearing in Carbon Nanofibers as Structural Energy Storage Devices. *Adv. Funct. Mater.* **2019**, *29*, No. 1901425.

(15) Zhang, Y.; Mu, Z.; Lai, J.; Chao, Y.; Yang, Y.; Zhou, P.; Li, Y.; Yang, W.; Xia, Z.; Guo, S. MXene/Si@SiO_x@C Layer-by-Layer Superstructure with Autoadjustable Function for Superior Stable Lithium Storage. *ACS Nano* **2019**, *13*, 2167−2175.

(16) Tian, Y.; Yang, C.; Luo, Y.; Zhao, H.; Du, Y.; Kong, L. B.; Que, W. Understanding MXene-Based "Symmetric" Supercapacitors and Redox Electrolyte Energy Storage. *ACS Appl. Energy Mater.* **2020**, *3*, 5006−5014.

(17) Dillon, A. D.; Ghidiu, M. J.; Krick, A. L.; Griggs, J.; May, S. J.; Gogotsi, Y.; Barsoum, M. W.; Fafarman, A. T. Highly Conductive Optical Quality Solution-Processed Films of 2D Titanium Carbide. *Adv. Funct. Mater.* **2016**, *26*, 4162−4168.
(18) Lukatskaya, M. R.; Kota, S.; Lin, Z.; Zhao, M.-Q.; Shpigel, N.; Levi, M. D.; Halim, J.; Taberna, P.-L.; Barsoum, M. W.; Simon, P.; Gogotsi, Y. Ultra-high-Rate Pseudocapacitive Energy Storage in Two-dimensional Transition Metal Carbides. *Nat. Energy* **2017**, *2*, No. 17105.
(19) Zhang, C.; Anasori, B.; Seral-Ascaso, A.; Park, S. H.; McEvoy, N.; Shmeliov, A.; Duesberg, G. S.; Coleman, J. N.; Gogotsi, Y.; Nicolosi, V. Transparent, Flexible, and Conductive 2D Titanium Carbide (MXene) Films with High Volumetric Capacitance. *Adv. Mater.* **2017**, *29*, No. 1702678.
(20) An, H.; Habib, T.; Shah, S.; Gao, H.; Radovic, M.; Green, M. J.; Lutkenhaus, J. L. Surface-agnostic Highly Stretchable and Bendable Conductive MXene Multilayers. *Sci. Adv.* **2018**, *4*, No. eaaq0118.
(21) Zhao, M.-Q.; Ren, C. E.; Ling, Z.; Lukatskaya, M. R.; Zhang, C.; Van Aken, K. L.; Barsoum, M. W.; Gogotsi, Y. Flexible MXene/Carbon Nanotube Composite Paper with High Volumetric Capacitance. *Adv. Mater.* **2015**, *27*, 339−345.
(22) Yan, J.; Ren, C. E.; Maleski, K.; Hatter, C. B.; Anasori, B.; Urbankowski, P.; Sarycheva, A.; Gogotsi, Y. Flexible MXene/Graphene Films for Ultrafast Supercapacitors with Outstanding Volumetric Capacitance. *Adv. Funct. Mater.* **2017**, *27*, No. 1701264.
(23) Ke, Q.; Wang, J. Graphene-based Materials for Supercapacitor Electrodes − A review. *J. Materiomics* **2016**, *2*, 37−54.
(24) Zhou, T.; Wu, C.; Wang, Y.; Tomsia, A. P.; Li, M.; Saiz, E.; Fang, S.; Baughman, R. H.; Jiang, L.; Cheng, Q. Super-tough MXene-functionalized Graphene Sheets. *Nat. Commun.* **2020**, *11*, No. 2077.
(25) Fan, Z.; Wang, Y.; Xie, Z.; Wang, D.; Yuan, Y.; Kang, H.; Su, B.; Cheng, Z.; Liu, Y. Modified MXene/Holey Graphene Films for Advanced Supercapacitor Electrodes with Superior Energy Storage. *Adv. Sci.* **2018**, *5*, No. 1800750.
(26) Xu, S.; Wei, G.; Li, J.; Han, W.; Gogotsi, Y. Flexible MXene−graphene Electrodes with High Volumetric Capacitance for Integrated Co-cathode Energy Conversion/storage Devices. *J. Mater. Chem. A* **2017**, *5*, 17442−17451.
(27) Zhao, M.-Q.; Trainor, N.; Ren, C. E.; Torelli, M.; Anasori, B.; Gogotsi, Y. Scalable Manufacturing of Large and Flexible Sheets of MXene/Graphene Heterostructures. *Adv. Mater. Technol.* **2019**, *4*, No. 1800639.
(28) Seyedin, S.; Yanza, E. R. S.; Razal; Joselito, M. Knittable Energy Storing Fiber with High Volumetric Performance Made from Predominantly MXene Nanosheets. *J. Mater. Chem. A* **2017**, *5*, 24076−24082.
(29) Fu, J.; Yun, J.; Wu, S.; Li, L.; Yu, L.; Kim, K. H. Architecturally Robust Graphene-Encapsulated MXene Ti_2CT_x@Polyaniline Composite for High-Performance Pouch-Type Asymmetric Supercapacitor. *ACS Appl. Mater. Interfaces* **2018**, *10*, 34212−34221.
(30) Xiao, F.-X.; Pagliaro, M.; Xu, Y.-J.; Liu, B. Layer-by-layer Assembly of Versatile Nanoarchitectures with Diverse Dimensionality: A New Perspective for Rational Construction of Multilayer Assemblies. *Chem. Soc. Rev.* **2016**, *45*, 3088−3121.
(31) Ahn, E.; Lee, T.; Gu, M.; Park, M.; Min, S. H.; Kim, B.-S. Layer-by-Layer Assembly for Graphene-Based Multilayer Nanocomposites: The Field Manual. *Chem. Mater.* **2017**, *29*, 69−79.
(32) Decher, G. Fuzzy Nanoassemblies: Toward Layered Polymeric Multicomposites. *Science* **1997**, *277*, 1232.
(33) Xiao, F.-X.; Zeng, Z.; Liu, B. Correction to "Bridging the Gap: Electron Relay and Plasmonic Sensitization of Metal Nanocrystals for Metal Clusters". *J. Am. Chem. Soc.* **2015**, *137*, 13990.
(34) Zhang, J.; Xiao, F.-X. Modulation of Interfacial Charge Transfer by Self-assembly of Single-layer Graphene Enwrapped One-dimensional Semiconductors Toward Photoredox Catalysis. *J. Mater. Chem. A* **2017**, *5*, 23681−23693.
(35) Richardson, J. J.; Björnmalm, M.; Caruso, F. Technology-driven Layer-by-layer Assembly of Nanofilms. *Science* **2015**, *348*, No. aaa2491.
(36) Zhao, X.; Vashisth, A.; Prehn, E.; Sun, W.; Shah, S. A.; Habib, T.; Chen, Y.; Tan, Z.; Lutkenhaus, J. L.; Radovic, M.; Green, M. J. Antioxidants Unlock Shelf-Stable $Ti_3C_2T_x$ (MXene) Nanosheet Dispersions. *Matter* **2019**, *1*, 513−526.
(37) Zhang, L.; Su, W.; Huang, Y.; Li, H.; Fu, L.; Song, K.; Huang, X.; Yu, J.; Lin, C.-T. In Situ High-Pressure X-ray Diffraction and Raman Spectroscopy Study of $Ti_3C_2T_x$ MXene. *Nanoscale Res. Lett.* **2018**, *13*, No. 343.
(38) Li, X.; Yin, X.; Han, M.; Song, C.; Xu, H.; Hou, Z.; Zhang, L.; Cheng, L. Ti_3C_2 MXenes Modified with In Situ Grown Carbon Nanotubes for Enhanced Electromagnetic Wave Absorption Properties. *J. Mater. Chem. C* **2017**, *5*, 4068−4074.
(39) Hong, T.-K.; Lee, D. W.; Choi, H. J.; Shin, H. S.; Kim, B.-S. Transparent, Flexible Conducting Hybrid Multilayer Thin Films of Multiwalled Carbon Nanotubes with Graphene Nanosheets. *ACS Nano* **2010**, *4*, 3861−3868.
(40) Dong, W.; Ren, Y.; Zhang, Y.; Chen, Y.; Zhang, C.; Bai, Z.; Ma, R.; Chen, Q. Synthesis of Pb Nanowires-Au Nanoparticles Nanostructure Decorated with Reduced Graphene Oxide for Electrochemical Sensing. *Talanta* **2017**, *165*, 604−611.
(41) Long, L.; Wang, S.; Xiao, M.; Meng, Y. Polymer Electrolytes for Lithium Polymer Batteries. *J. Mater. Chem. A* **2016**, *4*, 10038−10069.
(42) Skunik, M.; Kulesza, P. J.; Vlachopoulos, N.; Häggman, L.; Hagfeldt, A. Development of Hybrid Organic-Inorganic Materials for Efficient Charging/Discharging in Electrochemical and Photoelectrochemical Capacitors. *ECS Trans.* **2019**, *35*, 93−102.
(43) Sun, D.; Wang, M.; Li, Z.; Fan, G.; Fan, L.-Z.; Zhou, A. Two-dimensional Ti_3C_2 as Anode Material for Li-ion Batteries. *Electrochem. Commun.* **2014**, *47*, 80−83.
(44) Sathiya, M.; Prakash, A. S.; Ramesha, K.; Tarascon, J. M.; Shukla, A. K. V_2O_5-Anchored Carbon Nanotubes for Enhanced Electrochemical Energy Storage. *J. Am. Chem. Soc.* **2011**, *133*, 16291−16299.
(45) Ardizzone, S.; Fregonara, G.; Trasatti, S. "Inner" and "outer" Active Surface of RuO_2 Electrodes. *Electrochim. Acta* **1990**, *35*, 263−267.
(46) Chew, K. W.; Chen, S. S.; Pang, W. L.; Tan, C. G.; Osman, Z. et al. In The Effects of Lithium Triflate ($LiCF_3SO_3$) on the PMMA-based Solid Polymer Electrolytes, *AIP Conference Proceedings*, 2010; pp 246−250.
(47) Song, Y.; Deng, P.; Qin, Z.; Feng, D.; Guo, D.; Sun, X.; Liu, X.-X. A polyanionic Molybdenophosphate Anode for a 2.7 V Aqueous Pseudocapacitor. *Nano Energy* **2019**, *65*, No. 104010.
(48) Chen, T.; Qiu, L.; Yang, Z.; Cai, Z.; Ren, J.; Li, H.; Lin, H.; Sun, X.; Peng, H. An Integrated "Energy Wire" for both Photoelectric Conversion and Energy Storage. *Angew. Chem., Int. Ed.* **2012**, *51*, 11977−11980.
(49) Wang, Z.; Cao, F.; Chen, K.; Yan, Y.; Chen, Y.; Zhang, Y.; Zhu, X.; Wei, B.; Xiong, Y.; Lv, Z. Cellular Structure Fabricated on Ni Wire by a Simple and Cost-Effective Direct-Flame Approach and Its Application in Fiber-Shaped Supercapacitors. *ChemSusChem* **2018**, *11*, 985−993.
(50) Meng, Q.; Wang, K.; Guo, W.; Fang, J.; Wei, Z.; She, X. Thread-like Supercapacitors Based on One-Step Spun Nanocomposite Yarns. *Small* **2014**, *10*, 3187−3193.
(51) Wang, Z.; Cheng, J.; Guan, Q.; Huang, H.; Li, Y.; Zhou, J.; Ni, W.; Wang, B.; He, S.; Peng, H. All-in-one Fiber for Stretchable Fiber-shaped Tandem Supercapacitors. *Nano Energy* **2018**, *45*, 210−219.
(52) Huang, Y.; Hu, H.; Huang, Y.; Zhu, M.; Meng, W.; Liu, C.; Pei, Z.; Hao, C.; Wang, Z.; Zhi, C. From Industrially Weavable and Knittable Highly Conductive Yarns to Large Wearable Energy Storage Textiles. *ACS Nano* **2015**, *9*, 4766−4775.
(53) Jeong, J.-H.; Park, J. W.; Lee, D. W.; Baughman, R. H.; Kim, S. J. Electrodeposition of α-MnO_2/γ-MnO_2 on Carbon Nanotube for Yarn Supercapacitor. *Sci. Rep.* **2019**, *9*, No. 11271.
(54) Gogotsi, Y.; Simon, P. True Performance Metrics in Electrochemical Energy Storage. *Science* **2011**, *334*, 917.

https://doi.org/10.1021/acsami.0c19619
ACS Appl. Mater. Interfaces 2021, 13, 14068−14076